Available online at www.sciencedirect.com
ScienceDirect
International Journal of Heat and Fluid Flow 28 (2007) 1204–1214
International Journal of HEAT AND FLUID FLOW
www.elsevier.com/locate/ijhff

DNS of passive scalar transport in turbulent channel flow at high Schmidt numbers

Florian Schwertfirm, Michael Manhart *

Fachgebiet Hydromechanik, Technische Universität München, Arcisstr. 21, 80337 München, Germany

Received 15 December 2006; received in revised form 9 May 2007; accepted 11 May 2007
Available online 2 August 2007

Abstract

We perform DNS of passive scalar transport in low Reynolds number turbulent channel flow at Schmidt numbers up to $Sc = 49$. The high resolutions required to resolve the scalar concentration fields at such Schmidt numbers are achieved by a hierarchical algorithm in which only the scalar fields are solved on the grid dictated by the Batchelor scale. The velocity fields are solved on coarser grids and prolonged by a conservative interpolation to the fine-grid.

The trends observed so far at lower Schmidt numbers $Sc \leqslant 10$ are confirmed, i.e. the mean scalar gradient steepens at the wall with increasing Schmidt number, the peaks of turbulent quantities increase and move towards the wall. The instantaneous scalar fields show a dramatic change. Observable structures get longer and thinner which is connected with the occurrence of steeper gradients, but the wall concentrations penetrate less deeply into the plateau in the core of the channel.

Our data shows that the thickness of the conductive sublayer, as defined by the intersection point of the linear with the logarithmic asymptote scales with $Sc^{-0.29}$. With this information it is possible to derive an expression for the dimensionless transfer coefficient K^+ which is only dependent on Sc and Re_τ. This expression is in full accordance to previous results which demonstrates that the thickness of the conductive sublayer is the dominating quantity for the mean scalar profile.

Keywords: DNS; Turbulent channel flow; Passive scalar; High Schmidt number; Mass transfer coefficient

1. Introduction

In recent years, direct numerical simulation (DNS) of low Reynolds number flows became readily available to the CFD community, providing reference data and insight for turbulent flow problems. A counter example is turbulent mixing, where the smallest length scale for turbulent mass transport η_B is related to the Kolmogorov scale by $\eta_B = \eta_K/Sc^{1/2}$ (Batchelor, 1959). For mixing of liquids, the Schmidt number Sc easily reaches values above $Sc = 1000$. Thus, DNS of scalar fields in such flows is still impossible with today's computer power, even at low Reynolds numbers.

A standard modelling approach for the turbulent mixing uses the eddy-diffusivity concept that requires the determination of a turbulent Schmidt number $Sc_t = \nu_t/\Gamma_t$. This number is either set to a constant value or determined by using a timescale ratio based on half the scalar variance and its dissipation rate. More sophisticated second order models solve the transport equations of the scalar fluxes (Johansson and Wikström, 1999). It has to be noted that with such a modelling, only large scale mixing can be modelled and the so-called micro mixing (i.e. mixing on a molecular level) is still out of reach. Due to the lack of DNS data for high Schmidt number flows most of these models have only been validated with $Sc \leqslant 1$ flows. The only detailed data on scalar transport at Schmidt numbers larger than 10 were obtained by DNS of a scalar with a mean gradient in isotropic turbulence performed by Brethouwer et al. (Brethouwer et al., 2003). To close these

* Corresponding author. Tel.: +49 8928922583; fax: +49 8928928332.
E-mail address: m.manhart@bv.tum.de (M. Manhart).

0142-727X/$ - see front matter © 2007 Elsevier Inc. All rights reserved.
doi:10.1016/j.ijheatfluidflow.2007.05.012

shortcomings, we consider the transport of a passive scalar quantity in fully developed turbulent channel flow at $Re_\tau = 180$ and Schmidt numbers of $Sc = 3$, 10, 25 and 49. This quantity could be either temperature or a concentration. From previous studies of this problem, it is known that the mass transfer coefficient K^+ decreases with increasing Schmidt (Prandtl) number with $K^+ = 0.0509 Sc^{-0.546}$ for $Sc < 10$ (Na et al., 1999) and $K^+ = 0.0889 Sc^{-0.704}$ for $Sc > 600$ (Papavassiliou and Hanratty, 1997; Shaw and Hanratty, 1977). This behaviour was corroborated by Mitrovic et al. (2004). These relations are hard to reconcile with the Taylor series approach. As in the near wall velocity profiles, there is a small near wall region in which turbulent transport can be neglected and the concentration profiles behave according to $Sc \cdot y^+$. The thickness of this conductive sublayer was given with $\Delta S \sim Sc^{-1/2}$ (Na et al., 1999; Na and Hanratty, 2000), $\Delta S \sim Sc^{-0.3}$ (Shaw and Hanratty, 1977) or $\Delta S \sim Sc^{-1/3}$ (Kader, 1981). In the present paper we develop a relation for K^+ which is only based on two conditions: the thickness of the conductive sublayer scales with $\Delta S \sim Sc^r$ and the concentration defect in the core of the channel is negligible.

In order to keep the numerical effort feasible, the domain size is slightly decreased compared to other simulations of this flow. A hierarchical grid was applied to save computational cost as the flow field could be computed on a coarser grid than the scalar field. At the highest $Sc = 49$, the scalar field was solved on 1.01×10^9 grid points.

In the next section, we outline the numerical method and describe the hierarchical grid algorithm. In Section 3, results are presented for the statistical quantities of the turbulent channel flow with mass transport and a scaling for the mean scalar field is developed. It is shown that with this scaling the dimensionless mass transfer coefficient can be predicted accurately for very high Sc. Section 4 contains a summary and conclusions.

2. Numerical method

A finite volume (FV) solver on a Cartesian grid with staggered variable arrangement was used for the computations (Manhart, 2004; Manhart and Friedrich, 2002). This scheme was modified by the following means. For the discretisation of the convective and diffusive fluxes at the cell faces an iterative explicit scheme of sixth order accuracy in the inner domain is used. Time integration is achieved by a third order Runge–Kutta method. The incompressibility constraint on the grid is satisfied by solving the Poisson-equation for the pressure with a second order incomplete Lower–Upper (ILU) decomposition and applying a correction step for the velocities. The solver uses a parallelisation by domain decomposition and runs on up to 210 cores of a Altix 4700.

2.1. Iterative explicit scheme

The resolution of steep gradients occurring in the concentration fields at high Schmidt numbers requires high resolution numerical approximations. A way to achieve higher resolution would be the use of higher order compact schemes (Lele, 1992). Unfortunately, these schemes come along with performance penalties when the resulting tridiagonal systems have to be solved on parallel computers. To avoid these penalties, we adopted an alternative approach to achieve a better resolution accuracy of the underlying numerical scheme. The flow solver is based on a conservative second order central scheme. For this scheme a filter transfer function G can be deduced which describes the relationship between the exact mathematical operator (e.g. first derivative) and the numerical operator (e.g. discrete numerical derivative). For example in the context of the modified wavenumber analysis, this filter G is the operator which relates the exact wavenumber k to the numerical wavenumber k^*. By constructing an approximate local filter in physical space to the filter G, inverting this filter with a series expansion and applying it to the field before the normal numerical operator is applied, a higher order approximation of the numerical operator can be constructed. In practice, this results in a repetitive application of an explicit filter with a successive application of the normal second order operator on the field, resulting in a sixth order explicit scheme. Due to the local and explicit formulation of all involved stencils an easy and straightforward parallelisation can be applied. For further details, see Schwertfirm et al. (accepted for publication).

2.2. Hierarchical grid

For $Sc > 1$ the length scales of the scalar field are smaller than the smallest length scales of the flow field, resulting in different resolution requirements for the flow and for the scalar fields. In a DNS the Kolmogorov length scale has to be resolved for the flow field and the Batchelor length scale for the scalar field. This means that the computation of the flow can be done on a coarser grid than the computation of the scalar. Therefore we implemented a hierarchical grid structure with a refinement factor of 2 in each direction. The grid for the scalar field is determined by the resolution requirement resulting from the Batchelor scale, hereafter called fine-grid. The flow is solved on a grid with double the cell sizes in each direction, hereafter called coarse-grid. We developed a conservative interpolation for non equidistant grids to determine the velocities on the fine-grid. This conservative interpolation has been designed (i) to conserve mass flux and (ii) to be second order accurate both on equidistant and non-equidistant grids.

Fig. 1 shows the 1D stencil for this interpolation in our staggered variable arrangement. The velocities U_i are on the coarse- and the velocities u_i on the fine-grid. In this schematic view only the coarse-grid finite volume cells are indicated. For the fine-grid velocities on the surfaces of each coarse-grid cell, following conditions are formulated: first the mass conservation

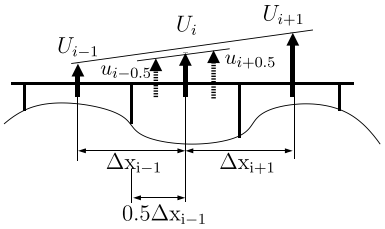

Fig. 1. Schematic view of the stencil for the conservative interpolation.

$$U_i \frac{1}{2}(\Delta x_{i-1} + \Delta x_{i+1}) = \frac{1}{2}(\Delta x_{i-1} u_{i-0.5} + \Delta x_{i+1} u_{i+0.5}), \tag{1}$$

and a second order formulation for the gradient

$$\frac{U_{i+1} - U_{i-1}}{\Delta x_{i-1} + \Delta x_{i+1}} = 4\frac{u_{i+0.5} - u_{i-0.5}}{\Delta x_{i-1} + \Delta x_{i+1}}. \tag{2}$$

Note that in our variable arrangement the fine-grid cell size is fixed as one half the distance between neighbouring coarse-grid velocities and that the velocities on the fine-grid are always stored in the middle of the fine-grid cell surface. Using these two equations successively for all three dimensions, the fine-grid velocities on the surface of one cube resulting from a coarse-grid cell can readily be determined. Moreover, when the coarse-grid velocities are divergence free, these fine-grid velocities are also divergence free. However, there are still 12 fine-grid velocities within this cube which still have to be calculated. These velocities are predicted by a second order central scheme. As those velocities are generally not mass conserving, an additional pressure correction step is performed to satisfy the continuity equation on each of the eight fine-grid cells resulting from the refinement of one coarse-grid cell. The pressure correction is formulated in a direct way. A Poisson-equation is set up for the eight fine-grid cells within the cube with Neumann boundary conditions for the pressure over the boundaries of this cube (as the velocities on the surface of this cube are already mass conserving). In a second order discrete formulation this results in eight equations with eight unknowns (e.g. the pressure values for each fine-grid cell):

$$\mathbf{A}\vec{p} = \vec{d} \tag{3}$$

where d is the divergence in each fine-grid cell. This system of equations is not linearly independent, so one pressure value is set to zero. The final 7×7 system can be solved directly as the matrix $\mathbf{A}$ is only dependent on the geometry, so that $\mathbf{A}^{-1}$ can be determined in a preprocessing step. The resulting pressure is used to correct the predicted fine-grid velocities. In this way the mass conservation is guaranteed for the fine-grid, even for non-equidistant grid spacings. Compared to a full DNS on the fine scalar grid, the computational savings are about a factor ≈ 7.

3. Results

All simulations were carried out in a fully developed turbulent channel flow at $Re_\tau = 180$, based on friction velocity u_τ, channel half width h and kinematic viscosity ν. Compared to other simulations of the turbulent channel flow (Kim et al., 1987; Na and Hanratty, 2000), the domain size was reduced to $(6.4h, 3.2h, 2h)$, which is the same as in Kawamura et al. (1998), in order to keep the computational effort feasible. The channel flow is periodic in the stream- and spanwise directions, hereafter referred as x- and y-direction. At the walls, there is a no-slip boundary condition for the velocities, whereas the scalar was added at the lower wall and removed at the upper wall by keeping the concentration constant at $c(x, y, 0) = 1.0$ and $c(x, y, 2h) = -1.0$. For the determination of the grid spacings, we adopted the following strategy. First, we evaluated the required resolutions for $Sc = 3$ by a grid study. We started with a grid spacing determined according to the relation $\eta_B = \eta_K/\sqrt{Sc}$, where η_K is the Kolmogorov and η_B the Batchelor length scale. The grid spacings required for a DNS of the flow field alone were known from other simulations (Schwertfirm and Manhart, 2005). We had to decrease the resulting fine-grid spacings by a factor of 1.875 in x- and 1.25 in y-direction in order to remove small spurious oscillations in the instantaneous scalar fields. The fine-grids for higher Sc were obtained by scaling this grid with $\sqrt{Sc}$. The spacings of the coarse-grids on which the flow fields were solved resulted from coarsening the fine-grids by a factor of 2 in each direction. For both grids the time step width used was determined from the CFL criteria of the find grid. Only one refinement level was implemented to keep the interpolation uncertainties small. The whole procedure resulted in the grids as stated in Table 1.

The coarse resolution for the $Sc = 3$ case is adequate to perform a DNS of the flow and scalar fields at $Sc = 1$ and this coarse-grid was also used to compute the scalar field at $Sc = 1$ for comparison.

To achieve a fast convergence of the scalar field, the different Sc cases were first computed on grid A as the computational effort was small and a large time step could be applied. From previous studies (Schwertfirm and Manhart, 2005) it was known that with the proper subgrid model the mean concentration field can be predicted quite accurately even for high Sc numbers. After the convergence of the scalar field was reached, e.g. the mean scalar field did not show any change from run to run, the data was interpolated on the Sc specific grid as a initial field. Starting from this solution each simulation was run for around $100t^*$ with $t^* = \nu/u_\tau^2$ (this corresponds to approximately 10 complete transitions of the channel with u_b) for the flow to fully develop before statistical sampling was started. The number of samples and the time covered with these samples are listed in Table 1 for each simulation.

3.1. Validation

To demonstrate the adequacy of the resolution of the flow field on velocity grid A, comparison of the rms of the velocities with reference data from Kim et al. (1987) are depicted in Fig. 2. Additionally the velocity rms

Table 1
Numerical grids used for the computations

Grid	A	B	C	D
Sc	3	10	25	49
Scalar resolution	$480 \times 200 \times 256$	$720 \times 300 \times 384$	$1200 \times 520 \times 640$	$1680 \times 672 \times 896$
Δx^+ scalar	2.4	1.6	0.96	0.68
Δy^+ scalar	2.88	1.92	1.1	0.85
Δz^+ scalar	0.67–2.49	0.45–1.67	0.25–1.05	0.18–0.75
$\eta_B^+(z^+ = 10)$	0.983	0.538	0.340	0.243
$\eta_B^+(z^+ = 180)$	2.097	1.148	0.726	0.519
Velocity resolution	$240 \times 100 \times 128$	$360 \times 150 \times 192$	$600 \times 260 \times 320$	$840 \times 336 \times 448$
Δx^+ velocity	4.8	3.2	1.92	1.37
Δy^+ velocity	5.76	3.84	2.2	1.7
Δz^+ velocity	1.35–4.98	0.9–3.34	0.50–2.1	0.36–1.5
Sample tv/u_b^2	6117	8743	2513	2734
Number of samples	3314	2526	1815	1481

sampled from the interpolated velocity fields of the fine-grid are plotted. The match of the data is very good, showing that the resolution for a DNS of the flow field is adequate on velocity grid A and that the interpolation of the velocities on the fine scalar grid is not introducing observable numerical noise.

On the right of Fig. 2 the velocity rms for velocity grids A–C are presented. The little differences indicate that the statistics are not yet fully converged, but nevertheless the curves show a good agreement.

In Fig. 3, the one dimensional energy spectra in the streamwise direction in the centre of the channel are plotted for the u velocity and for the scalar at different Sc. The u spectrum is taken from the coarse and the fine-grid of simulation B. In the wave numbers which are captured by the coarse grid, the interpolation does not introduce any noise and the spectra from the fine and the coarse grid are identical. The scalar spectra for the different Sc shows an increase in the energy content of higher wave numbers

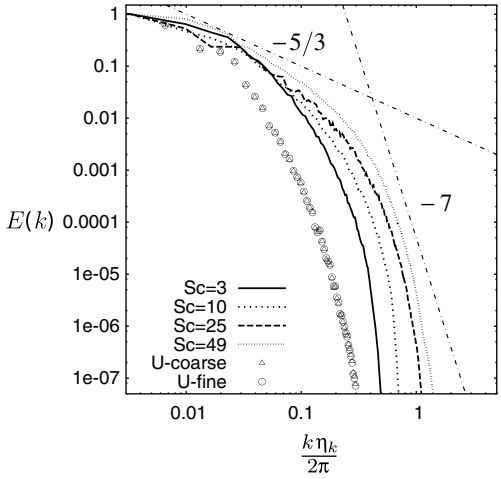

Fig. 3. One dimensional scalar energy spectra (lines) and one dimensional energy spectrum of the u velocity (symbols) in streamwise direction at $z^+ = 180$ normalised by Kolmogorov scale and the amplitude of the first mode.

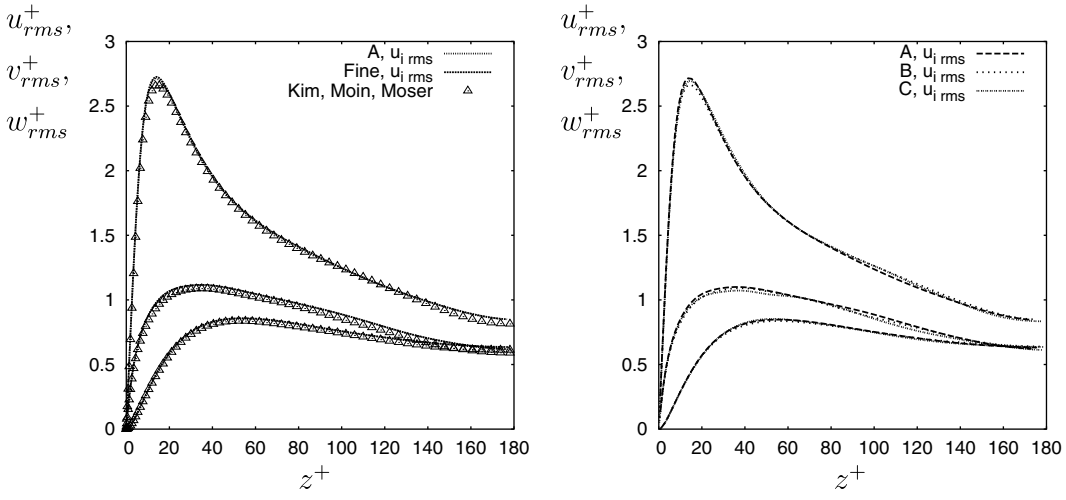

Fig. 2. Comparison of velocity rms-values. Grid A with reference data from Kim et al. (Kim et al., 1987) (left); comparison of grid A, B and C (right).

with increasing Sc. A smooth transition from the inertial range to the dissipative range is present where the dissipative range is well above the Batchelor scale. This indicates that all simulations are well resolved.

3.2. First and second order statistics

In Fig. 4 the mean scalar profiles (left) and the rms values of the scalar (right) are shown for $Sc = 1$–49. We use the normalisation with $c^+ = c/c_\tau$ and $c_\tau = (\frac{\Gamma}{u_\tau}\frac{\partial c}{\partial z})$. The data are compared to the high Sc data from Na (2005, 2000, 1999, symbols). Although the calculations from Na and Hanratty were carried out at $Re_\tau = 150$ the mean concentration profiles are very similar. Also the shapes and the trends in the concentration fluctuations are reproduced: with increasing Sc, the peak in the concentration fluctuations gets more pronounced and moves closer to the wall. The same trends were reported by Kawamura et al. (1998) for a channel at $Re_\tau = 180$ and uniform heating from both walls from $Sc = 0.025$ to $Sc = 5$.

Fig. 5 shows the turbulent mass fluxes, $\langle u'c'\rangle/(u_\tau c_\tau)$ and $\langle w'c'\rangle/(u_\tau c_\tau)$, respectively. We observe a similar trend as with the scalar rms, i.e. with increasing Sc, the peaks of the normalised turbulent mass fluxes in streamwise direction increase and move towards the wall. The wall normal turbulent mass fluxes tend towards unity in the core of the flow, as they are normalised by the wall mass flux, which is the sum of turbulent and diffusive fluxes. This means, that the contribution of the diffusive fluxes to the whole flux tends to zero in the core of the flow. The layer in which there is a significant diffusive contribution to the total mass flux, i.e. the diffusive sublayer, gets thinner with increasing Sc. The statistics of the vertical turbulent mass fluxes in the core of the channel are very slow to converge. Especially at $Sc = 25$ the statistics of this quantity are not yet fully converged, as indicated by the fact that there are values lower than at $Sc = 3$ in the middle of the channel. Nevertheless our data for $\langle c\rangle$ and $\langle c'w'\rangle$ at $Sc = 25$ are compared in a recent publication of Bergant and Tiselj (2007) with data achieved by their method and yields a very good agreement.

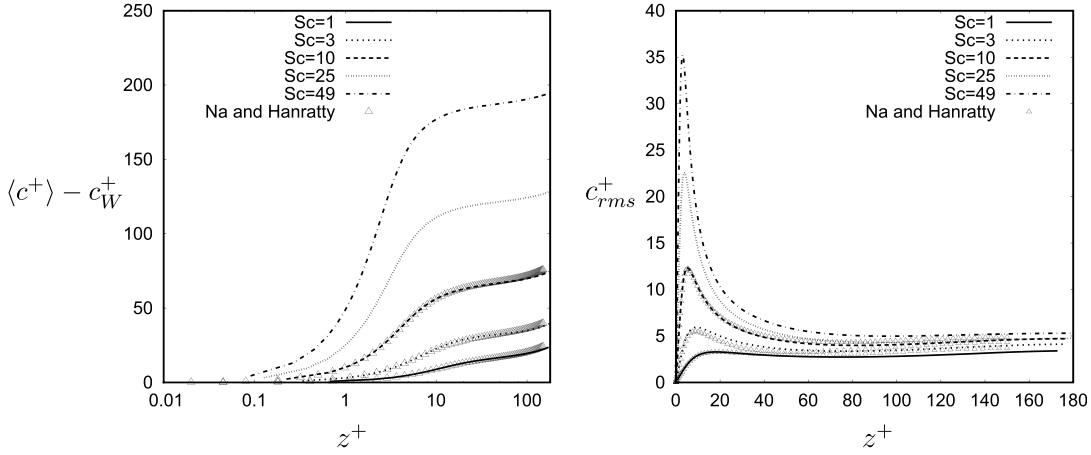

Fig. 4. Left: mean scalar field at different Sc; right: rms-value of the scalar at different Sc.

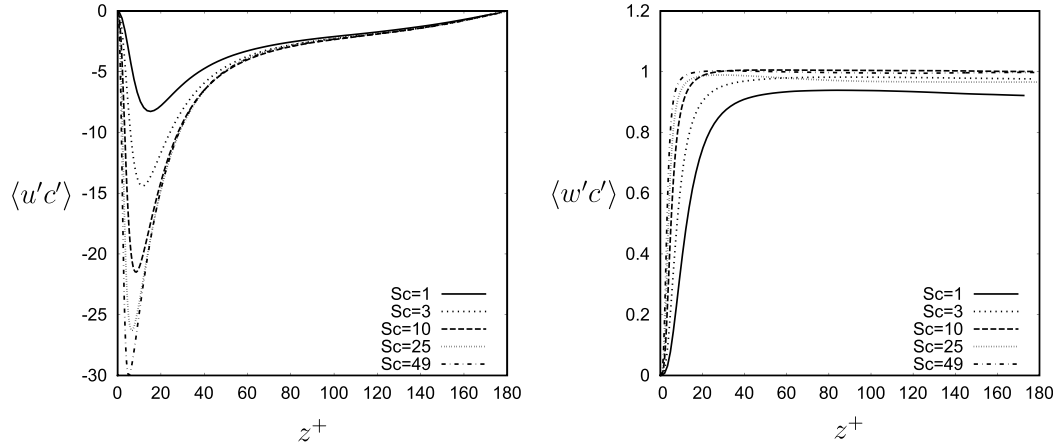

Fig. 5. Left: turbulent mass flux $\langle u'c'\rangle$ for different Sc.; Right: turbulent mass flux $\langle w'c'\rangle$ for different Sc (statistics for $Sc = 25$ and $Sc = 49$ not fully converged).

3.3. Instantaneous scalar fields

In the Figs. 6 and 7, instantaneous scalar fields at four different Sc in planes normal to the mainstream direction are shown. Most noticeable is the trend that structures get thinner and gradients get sharper with increasing Sc. As observed in the averaged quantities, the wall layer gets thinner and ejection events transport less mass into the core of the channel. This is reflected in the mean scalar gradient which tends to zero in the core of the channel with increasing Sc.

3.4. Transport equation for the scalar variance

The transport equation for the passive scalar variance in a constant density flow is given by:

$$\frac{\partial\langle c'^2\rangle}{\partial t}+\langle u_j\rangle\frac{\partial\langle c'^2\rangle}{\partial x_j}=-2\langle c'u_j'\rangle\frac{\partial\langle c\rangle}{\partial x_j}-2\Gamma\left\langle\left(\frac{\partial c'}{\partial x_j}\right)^2\right\rangle+\Gamma\frac{\partial^2\langle c'^2\rangle}{\partial x_j^2}-\frac{\partial\left\langle u_j'c'^2\right\rangle}{\partial x_j} \tag{4}$$

In a fully developed turbulent channel flow with homogeneous x- and y-direction, as it is the case here, the terms on the RHS of Eq. (4) simplify.

The production term is

$$P_c=-2\langle w'c'\rangle\frac{\partial\langle c\rangle}{\partial z}, \tag{5}$$

the dissipation term is:

$$\epsilon_c=-2\Gamma\left\langle\frac{\partial c'}{\partial x_j}\frac{\partial c'}{\partial x_j}\right\rangle \tag{6}$$

the turbulent diffusion term is

$$D_t=-\frac{\partial\langle w'c'^2\rangle}{\partial z}, \tag{7}$$

and the molecular diffusion term is

$$D_m=\Gamma\frac{\partial^2\langle c'c'\rangle}{\partial z^2}. \tag{8}$$

Figs. 8 and 9 show the terms of the transport equation for the scalar variance $\langle c'^2\rangle$ for $Sc=3$, 10, 25 and 49. As can be deduced from the transport equation for the mean scalar $\langle c\rangle$ in combination with Eq. (5), the peak of the production is $P_c^+=Sc/2$ for all Schmidt numbers, which was used to normalise the abscissa in the plots. In the core of the channel there is an approximate balance between production and dissipation for all Sc. At lower Sc, the turbulent and molecular diffusion are only relevant close to the wall. With increasing Sc ($Sc=10$–49) and close to the wall, D_t and D_m become more important and even comparative in magnitude with the dissipation term. This was also observed by Kawamura et al. for $Sc=5$. It is interesting to note that the turbulent diffusion term D_t gains importance with increasing Sc and is in the same order of magnitude (or even larger) than the production term between $20<z^+<80$ for $Sc=25$ and $Sc=49$, indicating that in this wall distance the main part of the scalar variance stems from turbulent transport.

3.5. Mixing and modelling

In what follows, we consider modelling of turbulent and molecular mixing at high Sc. An important quantity for

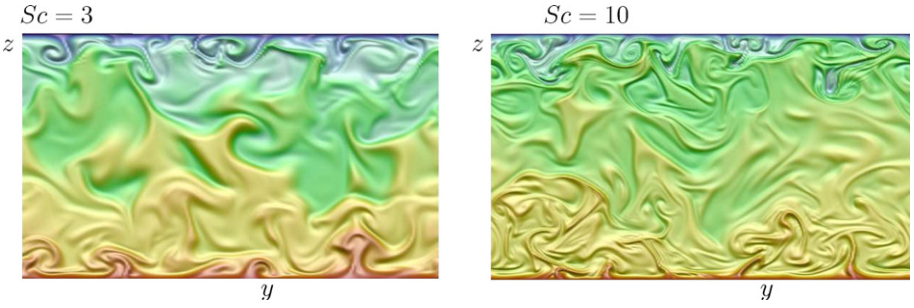

Fig. 6. Instantaneous scalar field in y–z-plane.

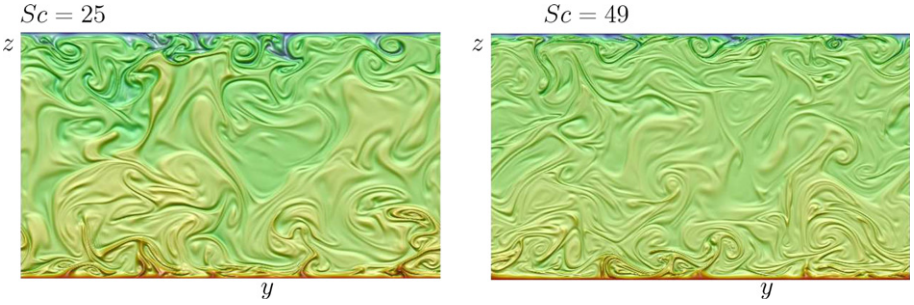

Fig. 7. Instantaneous scalar field in y–z-plane.

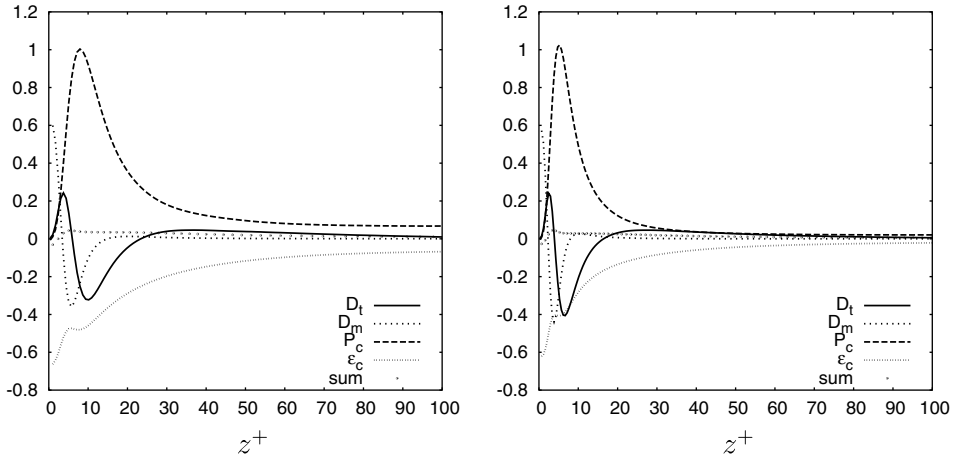

Fig. 8. Budget of the scalar variance transport equation, $Sc = 3$ left and $Sc = 10$ right.

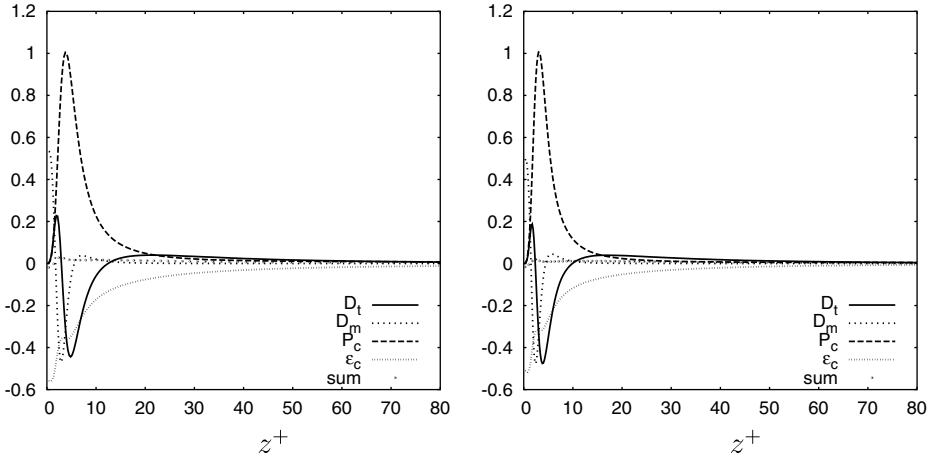

Fig. 9. Budget of the scalar variance transport equation, $Sc = 25$ left and $Sc = 49$ right.

modelling turbulent mixing and chemical reactions is the micromixing time. It is defined (Fox, 2003) as:

$$t_m = \frac{2\langle c'^2 \rangle}{\epsilon_c} \tag{9}$$

In the widely used IEM model for micromixing, a simple scale similarity approach (Corrsin, 1951; Fox, 2003) for the micromixing time is used:

$$\frac{\epsilon_c}{\langle c'^2 \rangle} = C_\Phi \frac{\epsilon}{k} \tag{10}$$

where k is the turbulent kinetic energy and ϵ its dissipation rate, with $C_\Phi \approx 2$ (Fox, 2003). A similar quantity, which was also reported by Kawamura et al. (1998) and Johansson and Wikström (1999) is the timescale ratio:

$$r = \frac{\langle c'^2 \rangle / \epsilon_c}{2k/\epsilon} \tag{11}$$

It is related to C_Φ according to $C_\Phi = 1/(2r)$. Both quantities, the micromixing time and the timescale ratio are depicted in Fig. 10. For a clearer view of the detailed structure close to the wall both plots are in double logarithmic scale.

The timescale ratio r (Fig. 10, left) approaches Sc at the wall, as was pointed out by Kawamura et al. (1998). It increases with increasing Sc. In the centre of the channel the timescale ratio clearly reaches values larger than one, e.g. $r = 2.53$ for $Sc = 49$. Therefore C_Φ ranges from 1/100 at the wall to ≈ 0.2 in the centre of the channel for $Sc = 49$, and thus deviates strongly from the theoretically derived value of $C_\Phi = 2$ for isotropic turbulence at high Re and Sc.

The mixing time (Fig. 10, right) increases with increasing Sc as it is directly related to the time scale ratio and the turbulent quantities stay constant with constant Re_τ. These plots demonstrate that for inhomogeneous flows r (and therefore also C_Φ) can easily span several orders of magnitude from the wall to the core of the channel, depending on

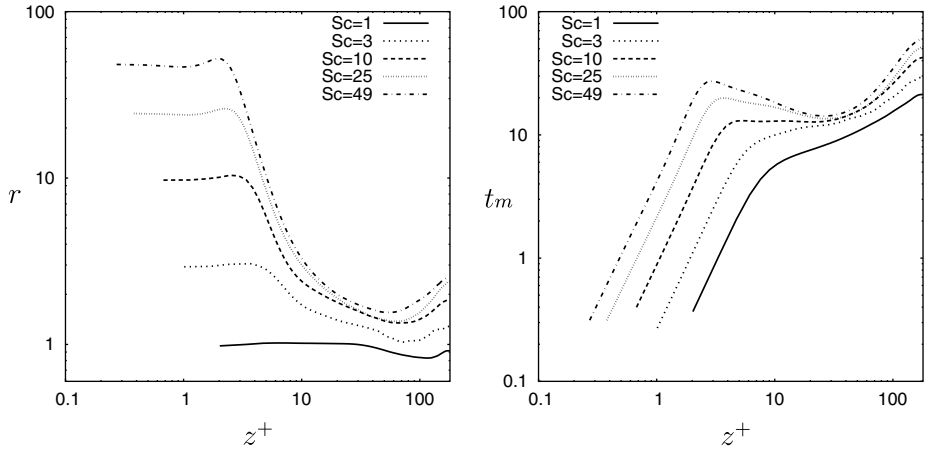

Fig. 10. Time sale ratio r (left) and micromixing time t_m (right) for various Sc.

the Schmidt number. Therefore, at least for the Reynolds numbers considered, the assumptions used to derive $C_\Phi = 2$ can not be made for this flow. Compared to the high Taylor-scale Reynolds numbers in the analytical derivation of the timescale ratio for a fully developed scalar spectrum and for spectral equilibrium of both, the scalar and the velocity spectrum (Fox, 2003), the Taylor-scale Reynolds number in the flow considered is much lower ($Re_\lambda = 25$ in the centre of the channel), and thus the discrepancy can be connected to the low Reynolds number. Therefore an adaption of C_Φ is necessary for flows with low local Reynolds numbers as pointed out already from Liu and Fox (2006).

Another important quantity for modelling is the turbulent Schmidt number $Sc_t = \frac{\nu_t}{\Gamma_t}$. There has been intensive discussion about the correct behaviour of Sc_t close to the wall. Antonia and Kim (1991) show that for $Sc \leqslant 2$, Sc_t approaches a value of $\approx$1.1 at the wall. This was also reported by Kawamura et al. (1998) for Sc up to 5. In contrast Na et al. (Na et al., 1999) reported that the value of Γ_t in the limit $z \to 0$ decreases with increasing Sc. With a constant turbulent diffusivity ν_t this implies an increase of Sc_t. Seki et al. (2006) showed for $Sc \leqslant 2$ the same limit as Antonia and Kim, but observed an increase in Sc_t close to the wall for $Sc = 10$, because of the smaller cross correlation factor $R_{w'c'}$. The increase of Sc_t is only visible for $z^+ \leqslant 2$, which can be the reason that this effect was not observed by Kawamura et al. (1998) as his data are only plotted for $z^+ > 1.0$.

In Fig. 11 (left) the turbulent diffusivity normalised by z^{+3} and ν for different Sc is shown. In the outer region $z^+ > 20$ the data collapses for all Sc. Close to the wall, the turbulent diffusivity reduces with increasing Sc. The distance from the wall at which Γ_t starts to deviate from the $Sc = 3$ value increases with increasing Sc. At $Sc = 10$ this is around $z^+ \sim 3$, which matches the data presented by Na et al. (1999), whereas at $Sc = 49$ the deviation starts at $z^+ \sim 6$. In our simulation we were not able to cover the zone in which $\Gamma_t/z^{+3} = \text{const}$, as the thickness of this sublayer is smaller than $z^+ < 1$ at $Sc = 1$, reduces further with increasing Sc and is much thinner than the conductive sublayer (compare Fig. 12). Also shown in Fig. 11 (right) are profiles of the turbulent Schmidt number close to the wall. As expected from the discussion about the turbulent

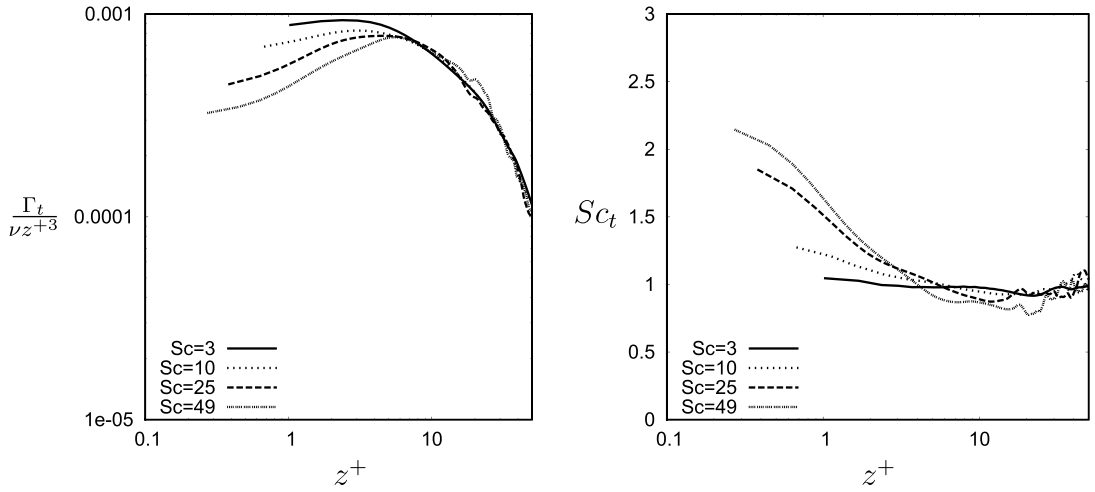

Fig. 11. Limiting behaviour of $\Gamma_t/(\nu z^{+3})$ (left) and Sc_t (right) for various Sc.

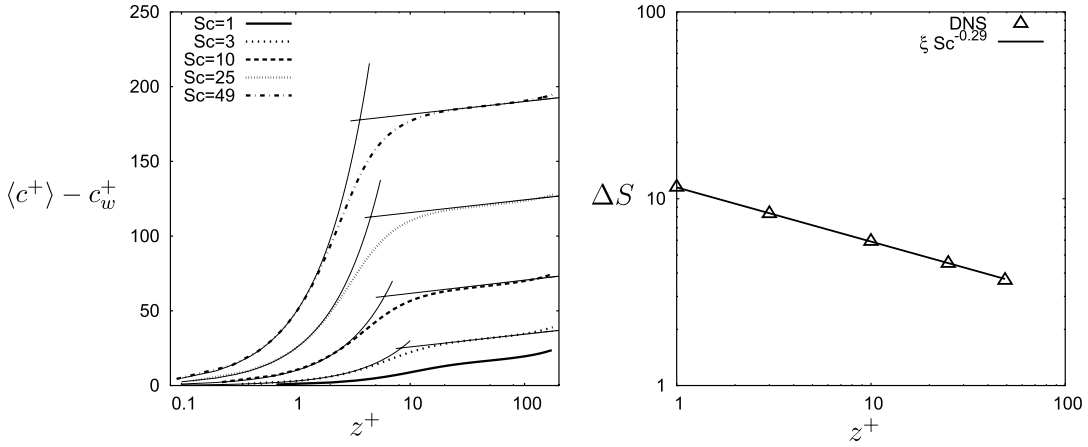

Fig. 12. Mean scalar profile with law of the wall (Eqs. (13) and (14)) (left); thickness of the conductive sublayer (right).

diffusivity, Sc_t increases with increasing Sc close to the wall. The values reach $Sc_t = 1.34$ at $Sc = 10$, which is similar to the result reported by Seki et al. and goes up to $Sc_t = 2.15$ at $Sc = 49$.

3.6. Scaling of the mean scalar field and mass transfer coefficient

In the fully developed turbulent channel flow the constant mass flux through the channel can be described by the dimensionless mass transfer coefficient K^+:

$$K^+ = \frac{1}{Sc}\frac{\partial c}{\partial z^+}\bigg|_W \frac{1}{c_W - c_C} = \frac{1}{\Delta c^+}, \tag{12}$$

where c_W is the wall concentration and c_C the centreline concentration. The dependency of K^+ on Sc has been subject to controversial discussion over the last decades (Le and Papavassiliou, 2006; Mitrovic et al., 2004; Shaw and Hanratty, 1977). Usually the relationship given is a power law $K^+ = CSc^b$ due to the analogy between momentum and heat transport. Depending on the assumption on the limiting behaviour of the turbulent diffusivity Γ_t close to the wall, the exponent can be derived as $b = -2/3$ or $b = -3/4$. Experimentally however, Shaw and Hanratty (1977) found the exponent to be $b = -0.704$ for high Sc and numerically Na et al. provided the relation $K^+ \sim Sc^{-0.546}$ for $1 < Sc < 10$ by DNS. These results imply that the analogy between momentum and mass transport does not hold for high Sc. Here, we develop an expression for $K^+(Sc)$ with the assumptions that the thickness of the conductive sublayer scales with $\Delta S \sim Sc^r$ and that the mean scalar profile follows the law of the wall with a linear and a logarithmic region. The law of the wall states that the mean scalar field scales linearly with z^+ in the conductive sublayer

$$\langle c^+\rangle - c_w^+ = Scz^+. \tag{13}$$

The logarithmic region is given by the equation

$$\langle c^+\rangle - c_w^+ = \frac{1}{\kappa_c}\ln z^+ + B_c. \tag{14}$$

To combine both relations and develop a general expression for the mean scalar profile, the thickness of the conductive sublayer must be known.

In Fig. 12 (left) we show the normalised mean scalar profiles along with the law of the wall, Eqs. (13) and (14), fitted to the data. By using the intersection point of these expressions we can define the thickness of the conductive sublayer ΔS. The coefficients κ_C and B_C fitted to the DNS data are summarised in Table 2 together with the thickness of the conductive sublayer.

In Fig. 12 (right), the thickneses of the conductive sublayers as described above are plotted over Sc in double logarithmic scale. The thickness scales with $\Delta S \sim Sc^{-0.29}$. This contradicts the result from Na et al., who reported a scaling of the thickness with $\Delta S \sim Sc^{-0.5}$ and is somewhat lower than $\sim Sc^{-1/3}$ which can be derived by Taylor series expansion (Kader, 1981). This difference may be due to the different definition as our intersection point lies somewhat outside the linear regime. On the other hand, Na et al. provide no clear definition of how the thickness was determined and a visual interpretation of the data gives unsatisfactory results. Why our empirical exponent is also lower than the one derived by the Taylor series analysis is an open issue and should be addressed in future work.

With the obtained parameters from Table 2, we can match the logarithmic region (Eq. (14)) with the linear regime at ΔS:

$$Sc\Delta S^+ = \frac{1}{\kappa_c}\ln \Delta_s^+ + B_c \tag{15}$$

Table 2
Parameters and thickness of the conductive sublayer layer extracted from the DNS

Sc	κ_C	B_C	ΔS
1	0.27	2.3	11.5
3	0.27	17.3	8.3
10	0.26	52.8	5.9
25	0.27	107.2	4.5
49	0.27	174.0	3.65

The position of the intersection point is only dependent on Sc:

$$\Delta S^+ = \xi Sc^{-0.29} \quad \text{with } \xi = 11.5 \quad \text{from } Sc = 1.0 \tag{16}$$

With Eq. (15) we can eliminate B_C from Eq. (14) and get an expression for the mean scalar profile in the logarithmic region:

$$\langle c^+ \rangle - c_w^+ = \frac{1}{\kappa_c} \ln z^+ + \xi Sc^{0.71} + \frac{0.29}{\kappa_c} \ln Sc - \frac{1}{\kappa_c} \ln \xi \tag{17}$$

As this equation is given in inner coordinates, Reynolds number effects are also mapped and we end up with a general description of the mean scalar profile in the logarithmic regime. It is dependent of the inner wall distance and Sc and requires only the empirically found parameters $\kappa_C = 0.27$, $\xi = 11.5$ and $r = 0.29$. The dimensionless mass transfer coefficient can now be determined with Eq. (12):

$$K^+ = \frac{1}{\frac{1}{0.27} \ln Re_\tau + 11.5 Sc^{0.71} + \frac{0.29}{0.27} \ln Sc - \frac{1}{0.27} \ln 11.5} \tag{18}$$

Fig. 13 (left) compares the expression $K^+ = 0.0889\, Sc^{-0.704}$ provided by Shaw and Hanratty (1977) for $600 < Sc < 36000$, the curve $K^+ = 0.0509 Sc^{-0.546}$ fitted through DNS data by Na et al. (1999), the results from our DNS simulations (symbols) as well as K^+ given by Eq. (18). The agreement between both empirical curves, the DNS results expression (12) is excellent. We see that that there is a smooth transition between the results from low to high Sc, i.e. Eq. (18) is able to describe the different exponents observed by various authors for low and high Schmidt numbers. Additionally, we have covered the dependency of K^+ on Re_τ. Changing Re_τ only effects K^+ at low Sc, as can be seen in Fig. 13 (right). At high Sc, K^+ becomes independent of Re_τ, and Eq. (18) reduces to $K^+ = 0.086957 Sc^{-0.71}$, which is very close to the relation given by Shaw and Hanratty. One has to note that at small Sc there is a slight deviation between our DNS simulations and expression (18). This is because we neglected the increased Δc^+ that is due to the influence of the velocity defect on the mean scalar field in the centre of the channel. As can be seen in Fig. 12 (left), the logarithmic profile underestimates the centreline concentration. The deviation reduces with increasing Sc. An interpretation of the shape of K^+ over Sc is straightforward. Within the conductive sublayer most of the change of the concentration takes place and its thickness in relation to the turbulent flow is responsible for the amount of scalar which will be transported across the channel by turbulent motions, e.g. by turbulent ejections. Once the conductive sublayer is considerable thinner than the viscous sublayer, at high Sc, the wall normal turbulent transport of quantity is reduced and the further development of K^+ only depends on the molecular diffusion and becomes independent of Re_τ.

4. Summary and conclusions

We performed DNS of passive scalar transport in fully developed turbulent channel flow at a low Reynolds number ($Re_\tau = 180$) and moderate Schmidt numbers up to $Sc = 49$. A high order Finite Volume scheme is used for the passive scalar transport equation. In order to keep the numerical effort feasible, a hierarchical grid structure was used that solves the Navier–Stokes equations only on a grid two times coarser than the passive scalar transport equation. By this, we reduced the computational effort by a factor of 7 without noticeable loss of accuracy. The averaged scalar fields and their second order statistics show a continuation of the trends observed so far in simulations at lower Schmidt numbers. Peaks move closer to the wall and the conductive sublayer gets thinner and thinner with increasing Sc. At $Sc = 25$, in almost 95% of the channel, the mass transport is done exclusively by turbulent transport. This is connected with the appearance of a concentration plateau in the core of the channel into which only few turbulent events are able to convect high (or respectively low) concentration fluid.

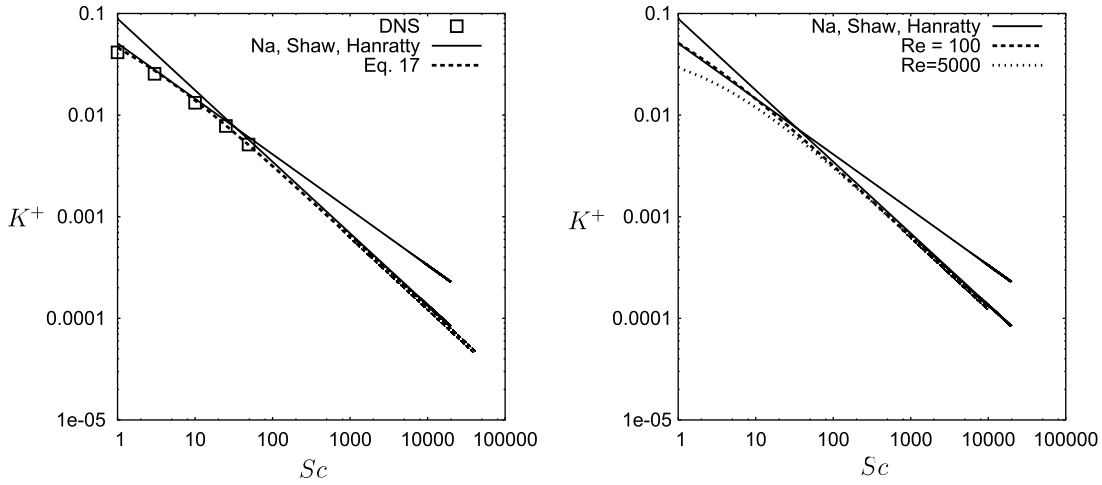

Fig. 13. Mass transfer coefficient over Sc at $Re_\tau = 180$ (left); mass transfer coefficient from Eq. (18) over Sc at $Re_\tau = 100$ and $Re_\tau = 5000$ (right).

Detailed analysis of the transport equation for the scalar variance revealed a growth in importance of the turbulent diffusion term in the range of $20 < z^+ < 80$, becoming even greater than the production term. The time scale ratio takes a wide range from the wall to the centre of the channel and is far from the often assumed value of $r = 1/4$ (or $C_\Phi = 2$, respectively) for high Re and Sc flows. Thus, for the inhomogeneous low Reynolds number flow considered, this assumption does not hold.

The DNS data shows that the limiting value of the turbulent diffusivity close to the wall reduces with increasing Sc and therefore the turbulent Schmidt number Sc_t increases. The layer, where $\Gamma_t \approx z^{+3}$, is much thinner than the conductive sublayer and reduces further with increasing Sc. Since the turbulent transport becomes negligible in the limit $z^+ \to 0$, this scaling is not important for the mean concentration profile.

An expression for the mean scalar profile dependent on Sc and Re_τ was developed. With it, it is possible to predict K^+ and match experimental and numerical data for K^+ closely. The expression is based on the thickness of the conductive sublayer which was observed to scale with $\Delta S = 11.5 Sc^{-0.29}$. With this relation almost the same exponent b in the expression for K^+ as given by Shaw and Hanratty (1977) can be recovered in the limit of high Sc. This gives strong evidence to the conclusion, that the thickness of the conductive sublayer determines the scalar transport across wall parallel flows at high Sc. At this moment is is not clear, why the thickness of the conductive sublayer scales with $Sc^{-0.29}$ instead of the scaling implied by the conventional limiting behaviour analysis. This remains an open question and should be addressed in future work.

References

Antonia, R., Kim, J., 1991. Turbulent Prandtl number in the near-wall region of a turbulent channel flow. Int. J. Heat Mass Transfer 34 (7), 1905–1908.

Batchelor, G.K., 1959. Small-scale variation of convected quantities like temperature in turbulent fluid. Part 1. General discussion and the case of small conductivity. J. Fluid Mech. 5, 113–133.

Bergant, R., Tiselj, I., 2007. Near-wall passive scalar transport at high Prandtl numbers. Phys. Fluids. 19, in press.

Brethouwer, G., Hunt, J., Nieuwstadt, F., 2003. Micro-structure and Lagrangian statistics of the scalar field with a mean gradient in isotropic turbulence. J. Fluid Mech. 474, 193–225.

Corrsin, S., 1951. The decay of isotropic temperature fluctuations in an isotropic turbulence. J. Aeronaut. Sci. 18, 417.

Fox, R.O., 2003. Computational Models for Turbulent Reacting Flows. Cambridge University Press.

Johansson, A., Wikström, P., 1999. DNS and modelling of passive scalar transport in turbulent channel flow with a focus on scalar dissipation rate modelling. Flow Turbulence Combust. 63, 233–245.

Kader, B., 1981. Temperature and concentration profiles in fully turbulent boundary layers. Int. J. Heat Mass Transfer 24 (9), 1541–1544.

Kawamura, H., Ohsaka, K., Abe, H., Yamamoto, K., 1998. DNS of turbulent heat transfer in channel flow with low to medium-high Prandtl number fluid. Int. J. Heat Fluid Flow 19, 482–491.

Kim, J., Moin, P., Moser, R., 1987. Turbulence statistics in fully developed channel flow at low Reynolds number. J. Fluid Mech. 177, 133–166.

Le, P., Papavassiliou, D., 2006. Turbulent heat transfer in plane couette flow. J. Heat Transfer 128, 53–62.

Lele, S.K., 1992. Compact finite difference schemes with spectral-like resolution. J. Comput. Phys. 103, 16–42.

Liu, Y., Fox, R., 2006. CFD predictions for chemical processing in a confined impinging-jets reactor. AIChE J. 52 (2), 731–744.

Manhart, M., 2004. A zonal grid algorithm for DNS of turbulent boundary layers. Comput. Fluids 33 (3), 435–461.

Manhart, M., Friedrich, R., 2002. DNS of a turbulent boundary layer with separation. Int. J. Heat Fluid Flow 23 (5), 572–581.

Mitrovic, B., Le, P., Papavassiliou, D., 2004. On the Prandtl or Schmidt number dependence of the turbulent heat or mass transfer coefficient. Chem. Eng. Sci. 59, 543–555.

Na, Y., 2005. Private Communication.

Na, Y., Hanratty, T.J., 2000. Limiting behaviour of turbulent scalar transport close to a wall. Int. J. Heat Mass Transfer 43, 1749–1758.

Na, Y., Papavassiliou, D.V., Hanratty, T.J., 1999. Use of direct numerical simulation to study the effect of Prandtl number on temperature field. Int. J. Heat Fluid Flow 20, 187–195.

Papavassiliou, D., Hanratty, T.J., 1997. Transport of a passive scalar in a turbulent channel flow. Int. J. Heat Mass Transfer 40 (6), 1303–1311.

Schwertfirm, F., Manhart, M., 2005. ADM Modelling for semi-direct numerical simulation of turbulent mixing and mass transport. In: Humphrey, J., Gatski, T., Eaton, J., Friedrich, R., Kasagi, N., Leschziner, M. (Eds.), Turbulence and Shear Flow Phenomena. Williamsburg, USA, pp. 823–828.

Schwertfirm, F., Mathew, J., Manhart, M., accepted for publication. Improving spatial resolution characteristics of finite difference and finite volume schemes by approximate deconvolution pre-processing. Computers and Fluids.

Seki, Y., Iwamoto, K., Kawamura, H., 2006. Prandtl number effect on turbulence quantities through high spatial resolution dns of turbulent heat transfer in a channel flow. In: Hanjalic, K., Nagano, Y.S.J. (Eds.), Turbulence, Heat and Mass Transfer, 5. Springer, pp. 301–304.

Shaw, D.A., Hanratty, T.J., 1977. Turbulent mass transfer to a wall for large schmidt numbers. AIChE J. 23 (1), 28–37.